Loss of the proteostasis factor AIRAPL causes myeloid transformation by deregulating IGF-1 signaling

Fernando G Osorio[1], Clara Soria-Valles[1], Olaya Santiago-Fernández[1], Teresa Bernal[1,2], María Mittelbrunn[1,3,4], Enrique Colado[2], Francisco Rodríguez[1], Elena Bonzon-Kulichenko[5], Jesús Vázquez[5], Montserrat Porta-de-la-Riva[6,7], Julián Cerón[6], Antonio Fueyo[8], Juan Li[9,10], Anthony R Green[9–11], José M P Freije[1] & Carlos López-Otín[1]

AIRAPL (arsenite-inducible RNA-associated protein-like) is an evolutionarily conserved regulator of cellular proteostasis linked to longevity in nematodes, but its biological function in mammals is unknown[1–3]. We show herein that AIRAPL-deficient mice develop a fully-penetrant myeloproliferative neoplastic process. Proteomic analysis of AIRAPL-deficient mice revealed that this protein exerts its antineoplastic function through the regulation of the insulin/insulin-like growth factor 1 (IGF-1) signaling pathway. We demonstrate that AIRAPL interacts with newly synthesized insulin-related growth factor-1 receptor (IGF1R) polypeptides, promoting their ubiquitination and proteasome-mediated degradation. Accordingly, genetic and pharmacological IGF1R inhibitory strategies prevent the hematological disease found in AIRAPL-deficient mice as well as that in mice carrying the *Jak2*[V617F] mutation, thereby demonstrating the causal involvement of this pathway in the pathogenesis of myeloproliferative neoplasms[4–6]. Consistent with its proposed role as a tumor suppressor of myeloid transformation, AIRAPL expression is widely abrogated in human myeloproliferative disorders. Collectively, these findings support the oncogenic relevance of proteostasis deregulation in hematopoietic cells, and they unveil novel therapeutic targets for these frequent hematological neoplasias.

Protein homeostasis is essential for a proper response to cellular stress conditions[7]. Regulatory mechanisms of protein quality control preserve the stability and functionality of the cellular proteome[8–10], and they are frequently involved in cancer and aging[11,12]. In this regard, AIRAPL (encoded by *ZFAND2B*) is a highly conserved endoplasmic reticulum (ER) protein of unknown biological function, but inactivation of its ortholog in *Caenorhabditis elegans* (AIP-1) shortens lifespan as a result of proteostasis impairment[1].

We have generated *Zfand2b*^{−/−} mice using a 'knockout first' strategy[13] (**Supplementary Fig. 1**). *Zfand2b*^{−/−} mice experience a long period of illness, starting from 6 months to 1 year of age, which is characterized by progressive weight loss, a distended abdomen and wasting (**Fig. 1a**) and results in premature death, with an average lifespan of 675 d (controls, 823 d, $P < 0.01$) (**Fig. 1b**). Necropsies of *Zfand2b*^{−/−} mice revealed a remarkable splenomegaly, resulting from extramedullary hematopoiesis and expansion of the myeloid lineage (**Fig. 1c,d** and **Supplementary Fig. 2a**). We also observed alterations in central hematopoiesis. Thus, bone marrow from *Zfand2b*^{−/−} mice started showing hypercellularity and trilineage hyperplasia but, at later stages, these mice presented with a remarkable reduction in cell number, trilineage dysplasia and myelofibrosis, as assessed by reticulin staining (**Fig. 1d**). Moreover, *Zfand2b*^{−/−} mice showed elevation in total leukocyte numbers in peripheral blood (**Fig. 1e**). Subsequently, we observed progressive myeloid skewing and a left-shifted myeloid maturation pattern in *Zfand2b*-knockout animals (**Supplementary Fig. 2b,c**). Notably, although we did not detect evidence of hematological disease in *Zfand2b*^{+/−} mice, we observed a substantial increase in myeloid cells, as compared to wild-type (WT; *Zfand2b*^{+/+}) mice (**Supplementary Fig. 2d**). Furthermore, compared to WT mice, hematocrit and platelets were also increased in *Zfand2b*^{−/−} mice (**Fig. 1f**). Overall, these phenotypes strongly support the occurrence of myeloproliferative neoplasms (MPNs)[4–6,14] in AIRAPL-deficient mice.

We next performed flow cytometry analysis of primitive Lin[−]SCA-1^{+}c-KIT[+] (LSK^{+}) cells and committed Lin[−]SCA-1^{−}c-KIT[+] (LSK[−]) progenitors. Notably, *Zfand2b*-knockout mice showed an increased number LSK^{+} cells, a loss of signaling lymphocyte activation molecule (SLAM)-enriched long-term hematopoietic stem cells (HSCs)[15] and an expansion of myeloid progenitors (**Fig. 1g** and **Supplementary Fig. 2e,f**). Furthermore, *Zfand2b*^{−/−} cells showed a competitive disadvantage over WT cells in repopulation assays (**Fig. 1h**)[16]. Additionally, we found a reduced number of myeloid

[1]Departamento de Bioquímica y Biología Molecular, Facultad de Medicina, Instituto Universitario de Oncología (IUOPA), Universidad de Oviedo, Oviedo, Spain. [2]Servicio de Hematología, Hospital Universitario Central de Asturias, Oviedo, Spain. [3]Instituto de Investigación Sanitaria, Hospital 12 de Octubre (i+12), Madrid, Spain. [4]Departamento de Bioquímica, Facultad de Medicina, Universidad Autónoma de Madrid (UAM), Madrid, Spain. [5]Laboratory of Cardiovascular Proteomics, Centro Nacional de Investigaciones Cardiovasculares, Madrid, Spain. [6]Area of Cancer and Human Molecular Genetics, Bellvitge Biomedical Research Institute (IDIBELL), L'Hospitalet de Llobregat, Barcelona, Spain. [7]*Caenorhabditis elegans* Facility, Bellvitge Biomedical Research Institute (IDIBELL), L'Hospitalet de Llobregat, Barcelona, Spain. [8]Área de Fisiología, Departamento de Biología Funcional, Facultad de Medicina, Universidad de Oviedo, Oviedo, Spain. [9]Wellcome Trust–Medical Research Council Stem Cell Institute, University of Cambridge, Cambridge, UK. [10]Department of Haematology, University of Cambridge, Cambridge, UK. [11]Department of Haematology, Addenbrooke's Hospital, Cambridge, UK. Correspondence should be addressed to C.L.-O. (clo@uniovi.es) or J.M.P.F. (jmpf@uniovi.es).

Figure 1 MPNs in *Zfand2b*-deficient mice.
(**a**) Representative picture of 18-month-old
WT (*Zfand2b+/+*) and *Zfand2b*-deficient mice.
Scale bar, 1.5 cm. (**b**) Kaplan-Meier survival plot
of *Zfand2b+/+* ($n = 20$) and *Zfand2b−/−* ($n = 28$)
mice. $P < 0.01$, log-rank/Mantel-Cox test.
(**c**) Mean spleen weights of *Zfand2b+/+*
($n = 8$) and *Zfand2b−/−* ($n = 8$) mice are represented.
(**d**) Representative images ($n = 8$) from
H&E staining of spleen and bone marrow
sections from age-matched WT and *Zfand2b*-
knockout mice. Scale bars, 500 μm (spleen)
and 25 μm (bone marrow). Black arrows indicate
reticulin fibers. (**e**,**f**) Cell counts of peripheral
blood from 1.5- and 18-month-old WT and
Zfand2b-knockout mice ($n = 20$ each condition).
WBC, white blood cell; Lym, lymphocyte;
Gra, granulocyte; Hct, hematocrit; Plt, platelet.
(**g**) Left, representative FACS analysis of SCA-1,
c-KIT and CD150 in bone marrow cells from
6-month-old *Zfand2b+/+* ($n = 7$) and *Zfand2b−/−*
($n = 7$) mice. Right, the percentage and absolute
numbers of LSK+ and SLAM-enriched cells
($n = 7$ per group). Values are normalized to total
viable cellularity. (**h**) Competitive repopulation
assay. Plots represent the percentage of WT or
Zfand2b-deficient Ly-5.2 cells in peripheral
blood or bone marrow from recipient mice
($n = 10$). Error bars indicate s.e.m. (*$P < 0.05$;
**$P < 0.01$, two-tailed Student's *t*-test).
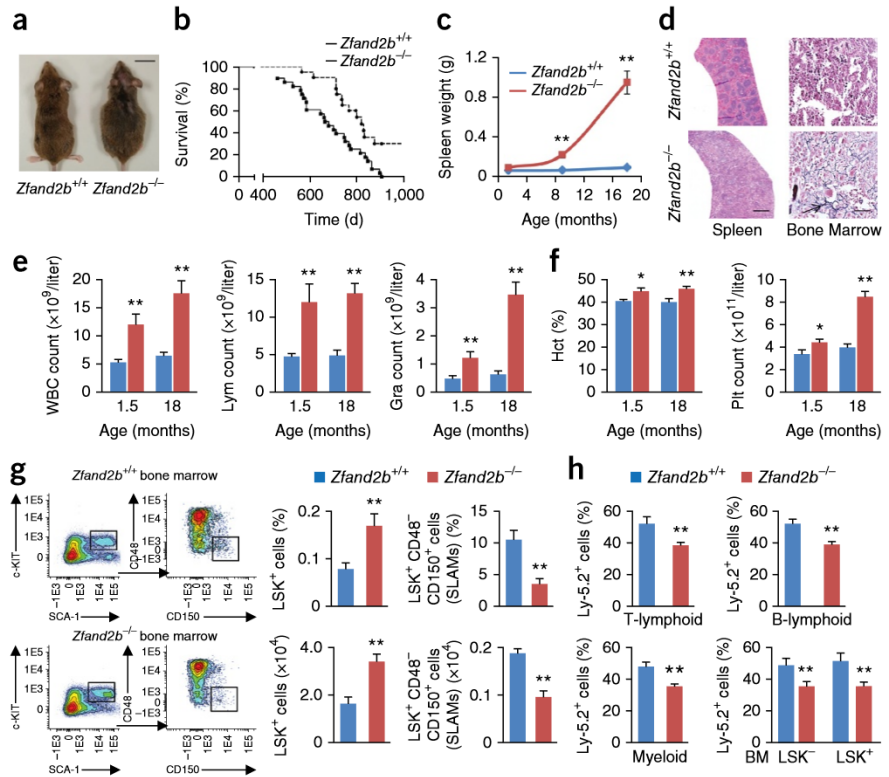
cells in bone marrow from mutant mice compared to marrow from WT mice (**Supplementary Fig. 2g**). Finally, reciprocal bone marrow transplantation experiments demonstrated the primary HSC defect caused by AIRAPL deficiency (**Supplementary Fig. 3**).

We performed exome sequencing of *Zfand2b−/−* polymorphonuclear cells (**Supplementary Table 1**). However, we did not observe any common sequence variants in genes associated with MPN pathogenesis, thereby supporting a driver role for AIRAPL deficiency in myeloid transformation in these mice. Thus, we analyzed ER stress response[17,18], but we observed no differences between *Zfand2b−/−* and WT mice in calreticulin expression or unfolded protein response (UPR) (**Supplementary Fig. 4**). Then, we studied JAK2 signaling in cells from *Zfand2b−/−* mice, as the activation of this pathway is a central feature of MPNs[19–21]. Nevertheless, we did not find differences between *Zfand2b−/−* and WT mice in JAK2 or STAT5 activation (**Supplementary Fig. 5a**), which prompted us to extend the analysis to other cellular kinases; we then observed a remarkable increase in IGF1R phosphorylation and activation of its targets in *Zfand2b−/−* mice relative to WT mice (**Fig. 2a** and **Supplementary Fig. 5b,c**)[22–24]. Total IGF1R levels were increased more than tenfold in *Zfand2b−/−* mice over those of WT mice (**Fig. 2a**,**b**), suggesting that the augmented activity of this receptor was caused by this increase.

To confirm these observations, we overexpressed AIRAPL in HEK-293T cells, observing a dose-dependent reduction in IGF1R levels compared to cells transfected with the empty vector, which was reverted by the proteasome inhibitor MG-132 (**Fig. 2c,d**), suggesting an ubiquitin-proteasome-mediated mechanism. Accordingly, AIRAPL overexpression induced IGF1R monoubiquitination (**Fig. 2e**). Moreover, AIRAPL co-immunoprecipitated with proteasome subunits and components of ER-associated degradation (ERAD) and preemptive quality-control (PQC) pathways, such as BAG6, FAF2 and VCP[25,26] (**Supplementary Fig. 6a** and **Supplementary Table 2**).

We obtained functional validation of these molecular partners through a genetic inhibitory strategy and identified a set of ER proteins essential for IGF1R degradation and ubiquitination, including VCP, FAF2, DERL1, BAG6 and the E3-ligase HERC2 (**Fig. 2f**).

IGF1R precursor (pro-IGF1R) is processed to yield both mature α-IGF1R and β-IGF1R chains. Cycloheximide-chase assays did not show differences between cells overexpressing AIRAPL and control cells in mature IGF1R degradation upon translation blockade, and pharmacological inhibition of the transport from ER to the Golgi apparatus did not affect AIRAPL function (**Supplementary Fig. 5d,e**), suggesting a regulatory role over nascent IGF1R. Moreover, even though mature IGF1R was approximately five times more abundant than its precursor, AIRAPL co-immunoprecipitated exclusively with pro-IGF1R (**Fig. 2g** and **Supplementary Fig. 5f,g**).

We next performed metabolic labeling with [35S]-methionine-cysteine to follow the fate of newly synthesized IGF1R. Because pro-IGF1R maturation occurs mostly at the Golgi apparatus[27], the analysis of pro-IGF1R processing can provide a temporal measurement of its translocation out of the ER. Analysis of HEK-293T cells overexpressing *ZFAND2B* revealed delayed translocation kinetics and lower amounts of translocated IGF1R (**Fig. 2h** and **Supplementary Fig. 5h**). To investigate the effect of endogenous AIRAPL on pro-IGF1R processing in human cells, we used a clustered regularly interspersed short palindromic repeats (CRISPR)-Cas9 approach to generate *ZFAND2B−/−* HEK-293T cells (**Supplementary Fig. 6b–d**). We found that *ZFAND2B*-knockout cells showed faster translocation kinetics and increased levels of mature IGF1R, as compared to WT cells (**Fig. 2i**). Altogether, these results demonstrate that AIRAPL controls nascent IGF1R translocation and degradation at the ER, thus regulating the steady-state levels of this receptor.

To test the specific contribution of IGF1R to the alterations caused by AIRAPL deficiency, we used a genetic strategy of *Igf1r* haploinsufficiency[28]. We generated *Zfand2b+/+Igf1r+/+*, *Zfand2b+/+Igf1r+/−*,

Figure 2 AIRAPL regulates IGF1R steady-state levels. (**a**) Western blot analyses of phospho-IGF1R (p-IGF1R) and total IGF1R in bone marrow from $Zfand2b^{+/+}$ (WT; $n = 5$) and $Zfand2b^{-/-}$ mice ($n = 5$). (**b**) IGF1R immunohistochemistry in spleens from WT and $Zfand2b^{-/-}$ mice. Scale bar, 50 μm. Numbers on the bars indicate values relative to WT controls. (**c**) Western blot analysis of IGF1R and AIRAPL in HEK-293T cells overexpressing AIRAPL ($n = 5$). (**d**) IGF1R western blot analysis in control (pcDNA3) and AIRAPL-transfected ($Zfand2b$) HEK-293T cells either treated or not with the proteasome inhibitor MG-132 (2 μM) ($n = 5$). β-actin was used as a loading control. (**e**) Hemagglutinin (HA)- and ubiquitin (P4D1 (mono-Ub) and FK1 (poly-Ub))-specific western blot analyses of GFP immunoprecipitates from HEK-293T cells transiently cotransfected with IGF1R-GFP and HA-ubiquitin plus either an AIRAPL cDNA ($Zfand2b$) or empty vector (pcDNA3). (**f**) Western blot analyses of IGF1R degradation (top) and ubiquitination (bottom) in HEK-293T cells, either transfected with pcDNA3.1 or AIRAPL, in the presence of specific siRNAs that target AIRAPL functional partners. (**g**) Western blot analysis of IGF1R

in total lysates and anti-HA-AIRAPL immunoprecipitates from HEK-293T cells transfected with HA-AIRAPL. Cells were treated with 5 μM MG-132 for 8 h before lysis. Mouse IgG was used as a negative control. (**h,i**) Metabolic labeling and anti-GFP immunoprecipitation of HEK-293T cells transiently transfected with IGF1R-GFP and either pcDNA3.1 or AIRAPL ($n = 5$) (**h**) or from $ZFAND2B^{+/+}$ and $ZFAND2B^{-/-}$ HEK-293T cells ($n = 5$) (**i**) (left). Western blot analyses of IGF1R and AIRAPL in total lysates from $ZFAND2B^{+/+}$ and $ZFAND2B^{-/-}$ HEK-293T cells (right). Signal intensities of western blot analyses and metabolic labeling experiments were quantified and mean values from at least three independent experiments are represented or indicated. Error bars indicate s.e.m. $**P < 0.01$, two-tailed Student's t-test.
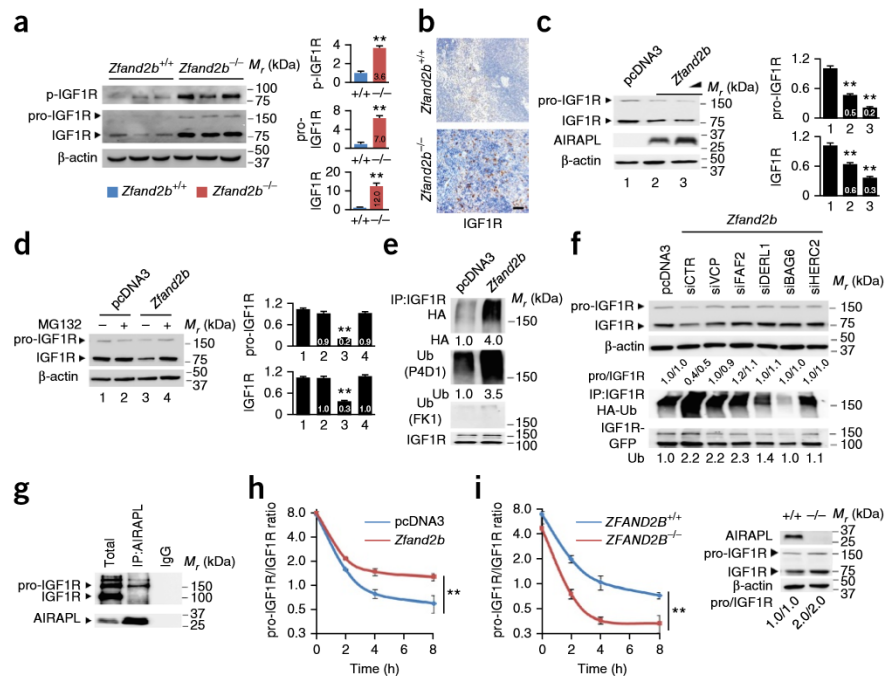
$Zfand2b^{-/-}Igf1r^{+/+}$ and $Zfand2b^{-/-}Igf1r^{+/-}$ mice, (**Supplementary Fig. 7a**), and we observed that $Igf1r$ haploinsufficiency prevented hematological alterations in $Zfand2b^{-/-}$ mice (**Fig. 3a–c** and

Supplementary Fig. 7a–c). Next, we tested the effect of the IGF1R kinase inhibitor NVP-AEW541 in $Zfand2b^{-/-}$ mice[29], and we saw a remarkable reversion of MPN-related alterations (**Fig. 3e–g** and

Figure 3 IGF1R inhibition prevents myeloproliferative neoplasms. (**a**) Peripheral blood cell counts in 6- and 12-month-old WT ($Zfand2b^{+/+}Igf1r^{+/+}$), $Zfand2b^{+/+}Igf1r^{+/-}$, $Zfand2b^{-/-}Igf1r^{+/+}$ and $Zfand2b^{-/-}Igf1r^{+/-}$ mice ($n = 10$ each genotype). (**b**) Representative photograph of spleens from 12-month-old mice of the indicated genotypes ($n = 6$ per genotype). Mean spleen weight values are shown. Scale bar, 1 cm. (**c**) Representative images from H&E staining of spleen and bone marrow sections from 12-month-old WT, $Zfand2b^{+/+}Igf1r^{+/-}$, $Zfand2b^{-/-}Igf1r^{+/+}$ and $Zfand2b^{-/-}Igf1r^{+/-}$ mice. Scale bars, 100 μm. Black arrows indicate reticulin fibers. (**d**) Graphs of FACS analysis of bone marrow from WT, $Zfand2b^{+/+}Igf1r^{+/-}$, $Zfand2b^{-/-}Igf1r^{+/+}$ and $Zfand2b^{-/-}Igf1r^{+/-}$ mice ($n = 5$ each genotype). Percentage (left) and absolute number (right) of LSK$^+$ cells are shown. (**e**) Cell counts of $Zfand2b^{-/-}$ mice before and after 1 or 2 months of daily NVP-AEW541 treatment ($n = 8$). (**f**) Mean spleen weight values of WT (blue), untreated (red) and 2-month-NVP-AEW541–treated (orange) $Zfand2b$-deficient mice ($n = 5$ per group). (**g**) Graphs of FACS analysis of bone marrow from WT ($n = 5$, blue), untreated ($n = 5$, red) and NVP-AEW541–treated ($n = 5$, orange)

$Zfand2b$-deficient mice. Percentage (left) and absolute number (right) of LSK$^+$ cells are shown. WBC, white blood cell; Lym, lymphocyte; Gra, granulocytes; Hct, hematocrit; Plt, platelet. Error bars indicate s.e.m. $*P < 0.05$; $**P < 0.01$, two-tailed Student's t-test.
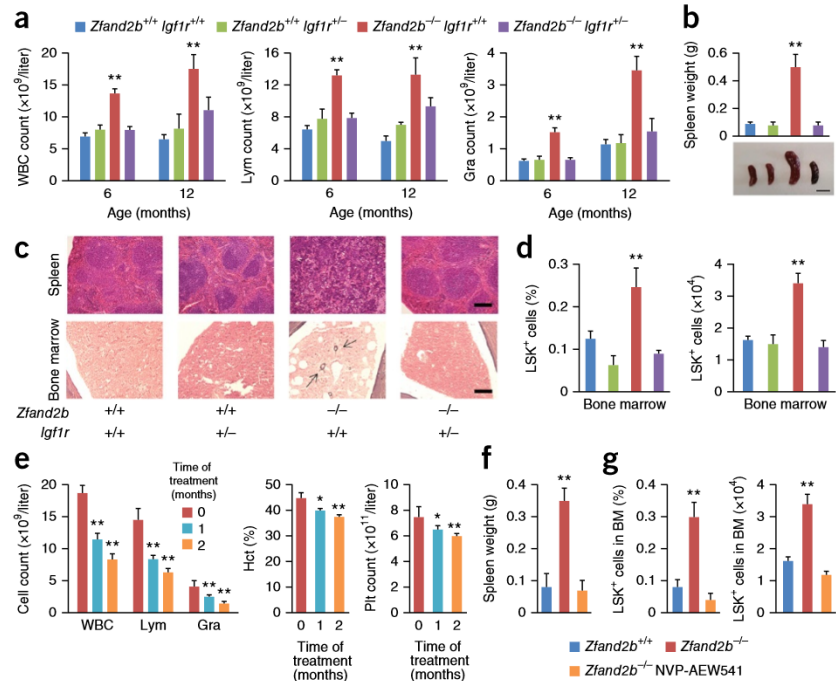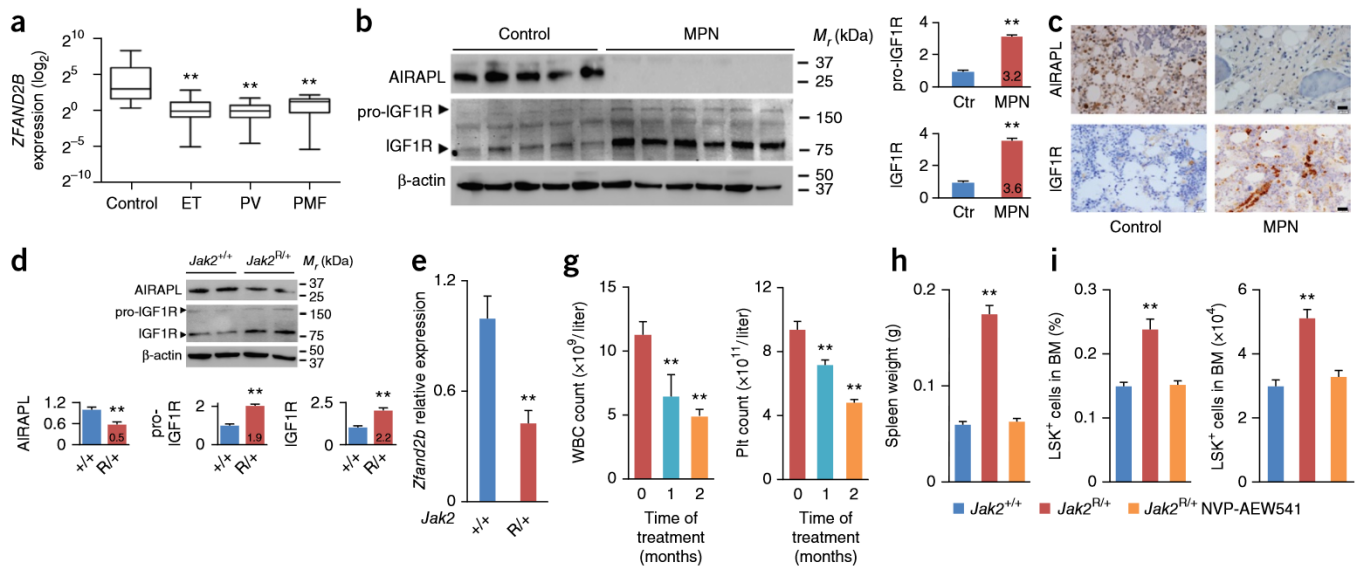
Figure 4 AIRAPL and IGF1R alterations in JAK2-driven MPN. (**a**) Box-whisker plot of *ZFAND2B* mRNA levels in human samples from controls ($n = 30$), ET ($n = 34$), PV ($n = 22$) and PMF ($n = 14$). $P < 0.01$, analysis of variance (ANOVA). (**b**) Western blot analysis of AIRAPL and IGF1R in MPN representative samples (ET ($n = 2$), PV ($n = 2$) and PMF ($n = 2$)) and controls. β-actin was used as a loading control. Numbers on the bars indicate values relative to controls. (**c**) Representative images of AIRAPL and IGF1R immunohistochemical analysis in bone marrow biopsies from MPN ($n = 30$) and controls ($n = 10$). Scale bars, 20 μm. (**d**) Western blot analysis of AIRAPL and IGF1R in $Jak2^{+/+}$ and $Jak2^{R/+}$ mice ($n = 5$ per group). (**e**) *Zfand2b* mRNA relative levels in bone marrow from $Jak2^{+/+}$ and $Jak2^{R/+}$ mice ($n = 5$ per group). (**f**) Gene set enrichment analysis (GSEA) plot comparing transcriptional profiles of hematopoietic stem cells (HSCs) from $Jak2^{R/+}$ and $Jak2^{+/+}$ mice. NES, normalized enrichment score. (**g**) Cell counts in peripheral blood from $Jak2^{R/+}$ before and after 1 or 2 months of daily NVP-AEW541 treatment. WBC, white blood cell; Plt: platelets; $n = 5$ per group. (**h**) Mean spleen weight values of $Jak2^{+/+}$, untreated and NVP-AEW541–treated $Jak2^{R/+}$ mice ($n = 5$ per group). (**i**) Graphs of FACS analysis of bone marrow from $Jak2^{+/+}$ ($n = 5$), untreated ($n = 5$) and NVP-AEW541–treated $Jak2^{R/+}$ mice ($n = 5$). LSK$^+$, Lin$^-$SCA-1$^+$c-KIT$^+$. (**j**) Relative proliferation with increasing concentrations of NVP-AEW541. Half-maximal inhibitory concentration (IC$_{50}$) values are indicated in SET2 and HEL cell lines. Signal intensities of western blot analyses were quantified and mean values from at least three independent experiments are represented or indicated. Error bars indicate s.e.m. $**P < 0.01$, two-tailed Student's t-test.

Supplementary Fig. 7f,g), which further implicated IGF1R in MPN pathogenesis caused by *Zfand2b* deficiency.

Next, we investigated the occurrence of AIRAPL alterations in 70 human samples from MPN types that are negative for the *BCR-ABL* fusion gene, including essential thrombocythemia (ET), polycythemia vera (PV) and primary myelofibrosis (PMF). We observed a notable *ZFAND2B* downregulation in these samples (**Fig. 4a** and **Supplementary Fig. 8a**). Protein analysis revealed a complete absence of AIRAPL in MPN samples, which correlated with a >3.5-fold increase in IGF1R levels relative to controls (**Fig. 4b**). Immunohistochemical analysis of bone marrow biopsies from MPN-affected individuals also revealed the absence of AIRAPL staining in myeloid cells (**Fig. 4c**).

To explore the relevance of AIRAPL and IGF1R in MPN pathogenesis, we used an mouse model of ET carrying the $Jak2^{V617F}$ mutation ($Jak2^{R/+}$ mice)[30]. Consistent with the results obtained in human MPN samples, we observed AIRAPL abrogation and IGF1R deregulation in $Jak2^{R/+}$ mice as compared to WT mice (**Fig. 4d–f**). Next, we administered

the IGF1R inhibitor NVP-AEW541 to $Jak2^{R/+}$ mice, and we observed the amelioration of MPN-associated characteristics (**Fig. 4g–i**). To further evaluate the role of IGF-1 signaling deregulation in JAK2-associated myeloid transformation, we transduced bone marrow cells from $Igf1r^{+/+}$ and $Igf1r^{+/-}$ mice with $Jak2^{V617F}$ cDNA, and injected them into WT mice. $Igf1r$ haploinsufficiency prevented the characteristic alterations associated with MPN (**Supplementary Fig. 8b–e**), providing evidence of the role of IGF-1 signaling in myeloid transformation.

We next analyzed the effect of IGF1R inhibition in two acute myeloid leukemia (AML) cell lines carrying the $JAK2^{V617F}$ mutation: SET2 and HEL. Both cell lines showed AIRAPL-dependent growth arrest upon IGF1R inhibition (**Fig. 4j**; **Supplementary Figs. 8f–h** and **9a**), whereas IGF1R overexpression increased proliferation relative to cells transduced with the empty vector (**Supplementary Fig. 9b**). Transcriptional profiling of SET2 and HEL cells transduced with a shRNA targeting *IGF1R* revealed specific repression of gene sets associated with AML transformation and downregulation of

JAK2-STAT5 signaling (**Supplementary Fig. 9c**). Conversely, JAK2 inhibition upregulated AIRAPL and reduced IGF1R levels compared to untreated cells, supporting the cross talk between these signaling pathways (**Supplementary Fig. 9d,e**).

Finally, we investigated the molecular mechanism responsible for *ZFAND2B* downregulation in MPNs. As we did not observe mutations, structural alterations or methylation changes in *ZFAND2B* in a variety of MPN types (**Supplementary Fig. 10a,b**)[17,18,31], we evaluated miRNA-mediated regulatory mechanisms. Computational searches identified miR-125a-3p as a potential regulator of *ZFAND2B*, and this role was confirmed by luciferase experiments that confirmed the capacity of this miRNA to target the *ZFAND2B* 3′ untranslated region (UTR) (**Supplementary Fig. 11a,b**). Notably, this miRNA was upregulated in MPN, and its expression was negatively correlated with that of *ZFAND2B* (**Supplementary Fig. 11c–f**). Moreover, we found that miR-125a-3p was altered in *Jak2*[V617F]-mutated mice (**Supplementary Fig. 11g–i**). The inhibition of miR-125a-3p in SET2 and HEL cells using a miR-125a 'sponge' reverted alterations associated to AIRAPL-deficiency (**Supplementary Fig. 12a–h**), supporting the causal implication of this regulatory pathway in MPN pathogenesis[32,33].

The reduced longevity of nematodes deficient for *aip-1*, encoding the worm ortholog of AIRAPL, suggested an evolutionarily conserved function of AIRAPL in insulin-IGF-1 signaling (IIS). To test this hypothesis, we generated *aip-1*–deficient worms on WT and *daf-2*–mutant (i.e., worms deficient for the IGFR ortholog *daf-2*) backgrounds (**Supplementary Fig. 13**). The longevity reduction of *aip-1*–deficient nematodes was abolished by deficiency in *daf-2*, thereby demonstrating a conserved role of AIRAPL in IIS regulation. Moreover, a purported role for AIRAPL in proinsulin peptide regulation at the ER has also been reported[34].

Collectively, the data shown herein demonstrate that AIRAPL acts as a suppressor of myeloid transformation through downregulation of IGF1R levels, demonstrating the involvement of insulin/IGF-1 signaling deregulation in myeloid malignancies[23,35]. Our studies showing the efficacy of IGF1R-inhibitory strategies in JAK2-driven MPNs support the use of IGF1R inhibitors for the treatment of these neoplasias, either alone or in combination with JAK2 inhibitors[36]. Furthermore, we have uncovered a novel mechanism of pathogenesis in human myeloproliferative disorders that involves the abrogation of AIRAPL tumor-suppressor activity through miR-125a-3p overexpression. On the basis of these findings, we propose that the identification of this novel pathway implicating AIRAPL, IGF1R and miR-125a-3p offers new opportunities for molecularly directed therapies against MPNs.

METHODS

Methods and any associated references are available in the online version of the paper.

Accession codes. RNA expression data are available at the Gene Expression Omnibus repository (GSE71922). Exome-sequencing raw data are accessible at the National Center for Biotechnology Information (NCBI) Sequence Read Archive (SRA) repository (SRP062260).

Note: Any Supplementary Information and Source Data files are available in the online version of the paper.

Reprints and permissions information is available online at http://www.nature.com/reprints/index.html.

1. Yun, C. *et al.* Proteasomal adaptation to environmental stress links resistance to proteotoxicity with longevity in *Caenorhabditis elegans*. *Proc. Natl. Acad. Sci. USA* **105**, 7094–7099 (2008).
2. Hassan, W.M., Merin, D.A., Fonte, V. & Link, C.D. AIP-1 ameliorates β-amyloid peptide toxicity in a *Caenorhabditis elegans* Alzheimer's disease model. *Hum. Mol. Genet.* **18**, 2739–2747 (2009).
3. Ferguson, A.A., Springer, M.G. & Fisher, A.L. *skn-1*–dependent and –independent regulation of *aip-1* expression following metabolic stress in *Caenorhabditis elegans*. *Mol. Cell. Biol.* **30**, 2651–2667 (2010).
4. Levine, R.L. & Gilliland, D.G. Myeloproliferative disorders. *Blood* **112**, 2190–2198 (2008).
5. Campbell, P.J. & Green, A.R. The myeloproliferative disorders. *N. Engl. J. Med.* **355**, 2452–2466 (2006).
6. Tefferi, A. & Vainchenker, W. Myeloproliferative neoplasms: molecular pathophysiology, essential clinical understanding and treatment strategies. *J. Clin. Oncol.* **29**, 573–582 (2011).
7. Balch, W.E., Morimoto, R.I., Dillin, A. & Kelly, J.W. Adapting proteostasis for disease intervention. *Science* **319**, 916–919 (2008).
8. Hartl, F.U., Bracher, A. & Hayer-Hartl, M. Molecular chaperones in protein folding and proteostasis. *Nature* **475**, 324–332 (2011).
9. Vembar, S.S. & Brodsky, J.L. One step at a time: endoplasmic reticulum–associated degradation. *Nat. Rev. Mol. Cell Biol.* **9**, 944–957 (2008).
10. Walter, P. & Ron, D. The unfolded protein response: from stress pathway to homeostatic regulation. *Science* **334**, 1081–1086 (2011).
11. López-Otín, C., Blasco, M.A., Partridge, L., Serrano, M. & Kroemer, G. The hallmarks of aging. *Cell* **153**, 1194–1217 (2013).
12. Hanahan, D. & Weinberg, R.A. Hallmarks of cancer: the next generation. *Cell* **144**, 646–674 (2011).
13. Skarnes, W.C. *et al.* A conditional knockout resource for the genome-wide study of mouse gene function. *Nature* **474**, 337–342 (2011).
14. Zhou, T., Kinney, M.C., Scott, L.M., Zinkel, S.S. & Rebel, V.I. Revisiting the case for genetically engineered mouse models in human myelodysplastic syndrome research. *Blood* **126**, 1057–1068 (2015).
15. Kiel, M.J. *et al.* SLAM family receptors distinguish hematopoietic stem and progenitor cells and reveal endothelial niches for stem cells. *Cell* **121**, 1109–1121 (2005).
16. Yildirim, E. *et al. Xist* RNA is a potent suppressor of hematologic cancer in mice. *Cell* **152**, 727–742 (2013).
17. Nangalia, J. *et al.* Somatic *CALR* mutations in myeloproliferative neoplasms with nonmutated *JAK2. N. Engl. J. Med.* **369**, 2391–2405 (2013).
18. Klampfl, T. *et al.* Somatic mutations of calreticulin in myeloproliferative neoplasms. *N. Engl. J. Med.* **369**, 2379–2390 (2013).

19. Levine, R.L. *et al.* Activating mutation in the tyrosine kinase JAK2 in polycythemia vera, essential thrombocythemia and myeloid metaplasia with myelofibrosis. *Cancer Cell* **7**, 387–397 (2005).
20. James, C. *et al.* A unique clonal *JAK2* mutation leading to constitutive signaling causes polycythaemia vera. *Nature* **434**, 1144–1148 (2005).
21. Baxter, E.J. *et al.* Acquired mutation of the tyrosine kinase JAK2 in human myeloproliferative disorders. *Lancet* **365**, 1054–1061 (2005).
22. Renehan, A.G. *et al.* Insulin-like growth factor (IGF)-I, IGF-binding protein 3 and cancer risk: systematic review and meta-regression analysis. *Lancet* **363**, 1346–1353 (2004).
23. Pollak, M. Insulin and insulin-like growth factor signaling in neoplasia. *Nat. Rev. Cancer* **8**, 915–928 (2008).
24. Gallagher, E.J. & LeRoith, D. Minireview: IGF, insulin and cancer. *Endocrinology* **152**, 2546–2551 (2011).
25. Glinka, T. *et al.* Signal peptide–mediated translocation is regulated by a p97-AIRAPL complex. *Biochem. J.* **457**, 253–261 (2014).
26. Kang, S.W. *et al.* Substrate-specific translocational attenuation during ER stress defines a pre-emptive quality control pathway. *Cell* **127**, 999–1013 (2006).
27. Khatib, A.M. *et al.* Inhibition of proprotein convertases is associated with loss of growth and tumorigenicity of HT-29 human colon carcinoma cells: importance of insulin-like growth factor 1 (IGF-1) receptor processing in IGF-1–mediated functions. *J. Biol. Chem.* **276**, 30686–30693 (2001).
28. Holzenberger, M. *et al.* IGF-1 receptor regulates lifespan and resistance to oxidative stress in mice. *Nature* **421**, 182–187 (2003).
29. García-Echeverría, C. *et al.* *In vivo* antitumor activity of NVP-AEW541–a novel, potent and selective inhibitor of the IGF-IR kinase. *Cancer Cell* **5**, 231–239 (2004).
30. Li, J. *et al. JAK2*^{V617F} homozygosity drives a phenotypic switch in myeloproliferative neoplasms but is insufficient to sustain disease. *Blood* **123**, 3139–3151 (2014).
31. Pérez, C. *et al.* Aberrant DNA methylation profile of chronic and transformed classic Philadelphia-negative myeloproliferative neoplasms. *Haematologica* **98**, 1414–1420 (2013).
32. Guo, S. *et al.* Complex oncogene dependence in microRNA-125a–induced myeloproliferative neoplasms. *Proc. Natl. Acad. Sci. USA* **109**, 16636–16641 (2012).
33. Inoue, D. *et al.* Myelodysplastic syndromes are induced by histone methylation–altering *ASXL1* mutations. *J. Clin. Invest.* **123**, 4627–4640 (2013).
34. Braunstein, I., Zach, L., Allan, S., Kalies, K.U. & Stanhill, A. Proteasomal degradation of preemptive quality control (pQC) substrates is mediated by an AIRAPL-p97 complex. *Mol. Biol. Cell* **26**, 3719–3727 (2015).
35. Lovly, C.M. *et al.* Rationale for cotargeting IGF-1R and ALK in ALK fusion–positive lung cancer. *Nat. Med.* **20**, 1027–1034 (2014).
36. Meyer, S.C. *et al.* CHZ868, a type II JAK2 inhibitor, reverses type I JAK inhibitor persistence and demonstrates efficacy in myeloproliferative neoplasms. *Cancer Cell* **28**, 15–28 (2015).

ONLINE METHODS

Mice. The gene-targeting vector for generation of the *Zfand2b*-'knockout first' allele was created through recombineering-specific methodology as previously described[13,37]. Briefly, a 12.7-kb fragment of mouse genomic DNA including the *Zfand2b* entire sequence was cloned into a pL253 vector, that contains the thymidine kinase gene for embryonic stem cell (ESC) negative selection. A *loxP* sequence was inserted into introns 1–2 of this gene along with a trapping element consisting of a splice acceptor sequence followed by a neomycin-resistance gene, which was used for positive selection of ESCs. The trapping element was flanked by FRT sites. Then, a second *loxP* site was inserted into introns 8–9 of the *Zfand2b* gene. Vector integrity was assessed by DNA sequencing and restriction mapping. The targeting vector was linearized and electroporated into the ESC line AB2.2 from the 129S5/SvEvBrd mouse strain. ESC clones were isolated after G418 and ganciclovir selection, and analyzed by Southern blotting for the identification of those clones that carried the targeted *Zfand2b*-knockout first allele. The probes detected a 7.2-kb fragment in the recombinant allele in XhoI-digested genomic DNA. Two different clones of targeted AB2.2 ESCs were microinjected into C57BL/6 mouse blastocysts to produce chimeric mice that were then subsequently crossed with C57BL/6 mice to generate *Zfand2b*-heterozygous mice. Mouse genotyping was performed by PCR of genomic DNA with the following oligonucleotides: 5′-gtgagcactggagctggaaa-3′; 5′-gtgggaaagggttcgaagtt-3′; 5′-cgcaaagctgctactcaggt-3′; The PCR products consisted in fragments of 254 bp (knockout allele) and 150 bp (WT allele). Conditional Jak2-V617F mice generation was previously described[30,38]. *Igf1r*-haploinsufficient mice were kindly provided by Dr. M. Holzenberger[28].

Mouse experiments. All of the animal experiments were conducted in accordance with the guidelines of the Committee for Animal Experimentation of the Universidad de Oviedo. Both male and female mice, carrying a mixed C57BL/6 × 129 background, were used in the experiments. For hematological determinations, blood was extracted directly from the mandibular sinus after anesthetizing mice with isoflurane. Blood samples were analyzed using Abacus junior vet equipment (Diatron Labs). For the experiments with an IGF1R small-molecule inhibitor, animals were administrated per os (p.o.) twice daily, 7 d/week with 50 mg/kg/d of NVP-AEW541, 10 ml/kg dissolved in 25 mM L(+)-tartaric acid. NVP-AEW541 was generously provided by Novartis. Tunicamycin (Sigma-Aldrich) was intraperitoneally injected into 8-week-old WT and *Zfand2b*-deficient mice at a dose of 1 μg/g body weight. Mice were euthanized 3 d after injection.

Human samples. Human MPN samples were collected from Hospital Universitario Central de Asturias (HUCA). The study was approved by the Ethical Committee of HUCA and all of the patients provided written informed consent. For *ZFAND2B* transcriptional analysis, 70 peripheral blood samples from MPN individuals and 30 controls were analyzed, and both male- and female-derived samples were collected and analyzed. For AIRAPL immunohistochemistry analysis, 30 samples from MPN bone marrow biopsies and 10 controls were collected. All the samples collected were included in the analysis.

***Caenorhabditis elegans* experiments.** Standard nematode growth medium and conditions were used for *C. elegans* growth and maintenance. The CB1370 [*daf-2*(e1370)III] and DH26 [*fer-15*(b26)] strains were obtained from the Caenorhabditis Genetics Center. Temperature sensitive *fer-15* (fertility) mutation was used to prevent the production of offspring that would confound the evaluation of adult worms. The GM6 [fer-15(b26) II/ daf-2(e1370) II] strain was a kind gift of Dr. Manuel J. Muñoz Ruiz. All worm populations were synchronized with the alkaline hypochlorite treatment[39]. To perform RNA-mediated interference (RNAi) by feeding, nematode growth medium (NGM) plates were supplemented with 50 μg/ml ampicillin, 12.5 μg/ml tetracycline, and 1 mM IPTG. Plates were seeded with the corresponding RNAi clone, validated by PCR and/or sequencing, and dsRNA synthesis induced o/n at 37 °C. The *aip-1* RNAi clone was obtained from the ORFeome library[40], while *daf-16* RNAi clone was from the Ahringer library[41]. Worms were grown on regular NGM plates and transferred to RNAi plates at L4 stage. For N2 and

daf-2(e1370) strains, plates were supplemented with 0.1 mg/ml fluorodeoxyuridine (FUDR) to prevent progeny growth and lifespan assays were conducted at 20 °C. For fer-15(b26) and fer-15(b26)/daf-2(e1370) strains, experiments were performed at 25 °C to avoid self-fertilization. At least 100 worms were used in each of the three experimental replicates. Animals were considered dead when no movement or pharyngeal pumping was observed after gentle touch to the head.

Bone marrow transplantation. Recipient mice were treated with 25 mg/kg/d of busulfan (Sigma-Aldrich) for 4 d, followed by injection of 200 mg/kg of cyclophosphamide (Sigma-Aldrich). 24 h after the last injection, bone marrow was collected from femurs and tibias of donor mice by flushing the cavity of freshly dissected bones with Hank's Balanced Salt Solution (HBSS, Gibco). Cell suspension was filtered through 100 μm filters and counted. 2×10^6 cells were resuspended in HBSS and then injected in recipient animals via the jugular vein. Eight weeks later, the engraftment was evaluated by qRT-PCR and immunofluorescence analyses of peripheral blood from recipient mice. In competitive transplantation experiments, cell populations were distinguished through the Ly-5.1 marker. 2×10^6 cells from mutant or WT littermates were mixed with 2×10^6 cells from B6.SJL-PtprcaPepcb/BoyJ (Ly-5.1$^+$) WT competitors and injected into mice recipients. Jak2-V617F transduction of bone marrow cells and subsequent transplantation of progenitors was performed as described previously[42]. Briefly, donor mice were treated for 5 d with 5-fluorouracil (150 mg/kg, intraperitoneal injection). Bone marrow cells were harvested and cultured for 24 h in transplant medium (RPMI 10% FBS, 6 ng/ml IL-3, 10 ng/ml IL-6, and 10 ng/ml stem cell factor). Then, cells were treated by spin infection with Jak2-V617F viral supernatants centrifuged at 1,800*g* for 30 min, 24 h before and on the day of transplantation. Whole BM cells (1×10^6) were resuspended in HBSS and injected into the jugular vein of busulfan/cyclophosphamide-treated mice.

FACS analysis. All the antibodies used in the study were from BioLegend unless noted. The following monoclonal antibodies were used for HSC analysis: PE anti-mouse CD117 (105807), PerCP/Cy5.5 anti-mouse CD45 (103132), PE/Cy7 anti-mouse CD150 (115914), APC anti-mouse CD127 (135012), APC/Cy7 anti-mouse CD48 (103432), Brilliant Violet 421 anti-mouse Ly-6A/E (Sca-1) (108127), FITC anti-mouse CD16/32 (101306), PE/Cy7 anti-mouse CD45.1 (110730), FITC anti-mouse CD45.2 (109806), Brilliant Violet 510 anti-mouse/human CD45R/B220 (103247), Brilliant Violet 421 anti-mouse CD3 (100227), anti-mouse CD34 (eBioscience, 11-0341-82), PE rat anti-mouse Ly-6G clone 1A8 (BD Pharmingen, 551461), APC rat anti-mouse Ly-6G and Ly-6C clone RB6-8C5 (BD Phamingen, 553129) and Lineage cocktail (BD Pharmingen, 558074). FACS data were acquired using a FACScanto II flow cytometer (BD Biosciences) and analyzed using Infinicyt software (Cytognos, Santa Marta, Spain).

Cell culture, transient transfection and viral transduction. *Zfand2b* cDNA was amplified by PCR and either cloned into pcDNA3.1-HA, pEGFP-C1, or pCDH expression vectors. pBABE-bleo IGF1R was obtained from Addgene, and then an IGF1R insert was subcloned into pEGFP-N1 or pCDH expression vector. miR-125a locus was amplified by PCR from human genomic DNA and cloned into pCDH. HA-ubiquitin plasmid was obtained from Addgene. miR-125 sponge was kindly provided by Dr. F.G. Wulczyn[43], and then subcloned into pCDH lentiviral vector. IGF1R shRNA were obtained from GE Dharmacon. WT and V617F Jak2 plasmids were previously described[44]. HEK-293T, SET2 and HEL cell lines were purchased from ATCC or DSMZ cell repositories and maintained in culture according to the provider's specifications. Transient transfections were performed using Lipofectamine reagent (Life Technologies). For lentiviral transduction, HEK-293T cells were transfected with pCDH-based vectors along with second-generation lentiviral packaging plasmids. Viral particles were collected from supernatants, filtered through 0.45 μm polyethersulfone (PES) filters and concentrated using Lenti-X concentrator reagent (Clontech). MG-132 was purchased from Sigma-Aldrich and used at a 2 μM concentration for the indicated times. Brefeldin A (Sigma-Aldrich) was used at 1 μg/ml for 8 h. Control and specific siRNAs were purchased from Life Technologies and transduced in HEK-293T using Lipofectamine reagent, and proteomic analyses were performed 48 h after transfection.

Western blot analysis. Protein lysates were prepared in RIPA buffer; equal amounts of total proteins were loaded onto SDS-polyacrylamide gels. After electrophoresis, gels were electrotransferred onto nitrocellulose membranes and incubated overnight with the different primary antibodies used. Finally, blots were incubated for 1 h with secondary antibodies conjugated with horseradish peroxidase (HRP) to develop immunoreactive bands. The primary antibodies used in the study were: AIRAPL (Atlas Antibodies, HPA035160), phospho-IGF1R (Novus, NB100-92555), IGF1R (Cell Signaling, 9750), β-actin (Sigma, AC-40), HA (Roche, 3F10), GFP (Clontech, 632592), phospho-AKT (Cell Signaling, 9275), AKT (Cell Signaling, 9272), phospho-S6K (Cell Signaling, 9430), S6K (Cell Signaling, 2708), phospho-4EBP1 (Cell Signaling, 9451), 4EBP1 (Cell Signaling, 9452), phospho-ERK (Cell Signaling, 9101), ERK (Cell Signaling, 9102), phospho-JAK2 (Cell Signaling, 3771), JAK2 (Cell Signaling, 3229), phospho-STAT5 (Cell Signaling, 9351), STAT5 (Cell Signaling, 9310), phospho-PERK (Cell Signaling, 3179), PERK (Cell Signaling, 5683), IRE1α (Cell Signaling, 3294), ATF6 (Santa Cruz Biotechnology, sc-22799), BiP (Cell Signaling, 3177), calreticulin (Abcam, 22683), VCP (Cell Signaling, 2648) and ubiquitin (Abcam, P4D1; Enzo, FK1). All the antibodies were used at a 1:1000 dilution unless noted. Mouse phospho–receptor tyrosine kinase (RTK) array was purchased from R&D systems and used according to the manufacturer's indications.

Immunoprecipitation. AIRAPL co-immunoprecipitation experiments were performed in the HEK-293T cell line. To this end, cells were transfected with either pEGFP-*Zfand2b* plasmid or pEGFP empty vector and incubated with MG-132, 8 h before lysis. Cells lysed with co-IP buffer (150 mM NaCl, 20 mM Tris-HCl pH 7.4, 1% NP-40, 1 mM MgCl$_2$, 10% glycerol, and complete protease inhibitors 1×). Protein extracts were precleared for 2 h at 4 °C with Dynabeads (Life Technologies), and then incubated with anti-GFP-conjugated Dynabeads for 1 h at 4 °C. Beads were washed three times with lysis buffer, and bound proteins were released from beads by boiling in 2× Laemmli sample buffer. Immunoprecipitates and input samples were resolved by SDS-PAGE or subjected to protein digestion followed by nano-liquid chromatography coupled to mass spectrometry for protein identification and quantification by peptide counting[45]. For ubiquitination experiments, HEK-293T cells were transfected with HA-ubiquitin, pcDNA3.1-HA-*Zfand2b* and pEGFP-IGF1R plasmids, and total lysates were precipitated with anti-GFP antibody and immunostained with anti-HA antibody. For cycloheximide chase, assayed cells were incubated with 100 µg/ml cycloheximide (Sigma-Aldrich) during the indicated times.

Pulse-chase metabolic labeling. 48 h after transfection with pEGFP-IGF1R construct, HEK-293T cells were incubated in cysteine- and methionine-free DMEM containing 10% dialyzed FBS for 12 h. Then, ^{35}S-labeled (0.1 mCi/ml; EasyTag Express35S Protein Labeling Mix; PerkinElmer) was added to the cells for 1 h. After labeling, cells were washed with chase medium (DMEM with 15 mg/l cold-methionine) and incubated in chase medium for the times indicated. Cells were then lysed in RIPA buffer, immunoprecipitated with anti-GFP antibody and resolved by SDS-PAGE. Nitrocellulose filters were exposed overnight and scanned using a Phosphorimager.

RNA. For quantitative RT-PCR (qRT-PCR), total RNA was isolated with Trizol and cDNA was synthesized with the ThermoScript RT-PCR system (Invitrogen). PCR was carried out in triplicate for each sample with 20 ng of cDNA using power SYBR Green PCR Master Mix (Applied Biosystems). Gene expression was normalized using *Gapdh* as endogenous control. The following oligonucleotides were used in the study; *Zfand2b*_fwd: 5′-AGGTCATCAGACCAGCAGGGCA-3′, *Zfand2b*_rev: 5′-GGTGTA GCTCTGCTTGGGGAGGAT-3′. Human *ZFAND2B* mRNA and miR-125a-3p levels were quantified with Taqman assays (Life Technologies), using β-actin and RNU6b, respectively as Taqman endogenous controls. Xbp1 splicing was analyzed by RT-PCR with the following oligonucleotides: mXbp1.3S: 5′-AAACAGAGTAGCAGCGCAGACTGC-3′, mXBP1.12AS: 5′-TCCTTCTGGGTAGACCTCTGGGAG-3′. PCR products were then digested with PstI and run in agarose gels. For microarray hybridization, double-stranded cDNA was synthesized using the SuperScript cDNA synthesis kit

(Invitrogen) and *in vitro* transcription was carried out with the Bioarray high yield RNA transcript labeling kit (Enzo Diagnostics). The biotin-labeled cRNA was purified, fragmented and hybridized to Human Gene 2.0 ST (Affymetrix). Washing and scanning were performed using a Fluidics Station 400 and GeneChip Scanner (Affymetrix). After scanning, raw data were processed with Expression Console software (Affymetrix), using default settings.

Histological analysis. Tissues were fixed in 4% buffered paraformaldehyde solution. Paraffin sections were stained with H&E or reticulin stains as noted. For immunohistochemical analysis, the following antibodies were used: myeloperoxidase (DAKO, A0398), CD3 (Abcam, 5690), Mac2 (Cedarlane, CL8942AP), AIRAPL (Atlas Antibodies, HPA035160) and IGF1R (Santa Cruz Biotechnology; sc-713). Blood smears were stained using May-Grünwald-Giemsa staining procedure. Reticulin fibers were revealed by silver staining according to the Gordon Sweet method. Histological analyses were performed in a blinded fashion.

Immunofluorescence analysis. Cells were fixed with 4% paraformaldehyde, rinsed in PBS, and permeabilized with 0.5% Triton X-100. Cells were then incubated with primary antibodies diluted in 10% FBS in PBS from 2 h at room temperature to overnight at 4 °C. After washing with PBS, cells were incubated with Alexa Fluor 488 (Life Technologies) conjugated secondary antibodies for 45 min at room temperature. Cells were counterstained with DAPI (Roche).

In vitro inhibitor assays. To assess the anti-proliferative effects of NVP-AEW541, SET2 and HEL cell lines were cultured at 10,000 cells/200 µl with increasing inhibitor concentrations in triplicate. Proliferation was assessed at 48 h using the Cell Titer 96 Non-Radioactive proliferation kit (Promega), and normalized to cell growth in media with an equivalent volume of DMSO. The concentration inhibiting proliferation by 50% (IC50) was determined with Graph Pad Prism 5.0. Ruxolitinib was obtained from Selleckchem.

Luciferase experiments. *ZFAND2B* 3′-UTR sequence was amplified by PCR and cloned into a psiCHECK2 vector downstream the *Renilla* luciferase sequence. Luminescence determinations were performed using the firefly luciferase values as an endogenous control. miR-125a-3p miRNA precursor and inhibitor were purchased from Life Technologies.

CRISPR-Cas9 experiments. Genome editing experiments were performed as described previously[46]. In brief, for the generation of *ZFAND2B*-deficient HEK-293T cells, two different plasmids encoding CRISPR-Cas9 and *ZFAND2B* guide RNA (gRNA) were obtained from Sigma-Aldrich (5544: 5′-GACCTCGGCGCTCACTGTTCGG-3′; 5545: 5′-CTCCGAACA CTGAGCGCCGAGG). gRNAs were selected to target *ZFAND2B* exon 1 in order to generate frameshift mutations that would cause premature termination of the open reading frame in this gene. CRISPR-Cas9 plasmids were transiently transduced into HEK-293T cells and clones were isolated by serial dilution. To analyze the resulting genomic DNA modifications induced by CRISPR-Cas9 activity, we amplified by PCR the targeted DNA region using external oligonucleotides. The forward oligonucleotide was modified to include 6-FAM fluorophore in its 5′ position, which allowed the fragment analysis of resulting PCR products by capillary electrophoresis. Indels were also confirmed by DNA sequencing. Three HEK-293T cell clones carrying deleterious modifications and three WT clones were selected for the experiments to rule out potential off-target effects of Cas9.

Exome sequencing and data analysis. Genomic DNA from bone marrow polymorphonuclear cells (200 ng) was sheared and used for the construction of a paired-end sequencing library as described in the protocol provided by Illumina. Enrichment of exonic sequences was then performed for each library using the SureSelectXT Mouse All Exon kit (Agilent) according to the manufacturer's instructions. Exon-enriched DNA was precipitated with magnetic beads coated with streptavidin (Invitrogen) and was washed and eluted. 18 additional cycles of amplification were then performed on the captured library. Enriched libraries were sequenced in two lanes of an Illumina Gene Analyzer IIx sequencer, using the standard protocol.

Data analysis and identification of sequence variants was performed using the Sidrón pipeline in a HD Genome One Research Edition station (DREAMgenics, Asturias, Spain)[47].

Gene set enrichment analysis. For data analysis, we used GSEA release 5 and MSigDB release 5 (http://www.broadinstitute.org/gsea/index.jsp). Weighted enrichment scores were calculated with gene expression lists ranked by signal to-noise ratio. The maximum gene set size was set to 500 genes; the minimum gene set size was set to 20 genes; the number of permutations was set to 1000. Selected enriched pathways had a relaxed false discovery rate of <0.25 and $P < 0.05$. GSEA shown in **Figure 4f** was performed with microarray data sets of a previous study[48]. Methylation and PMF cohorts analyses derived from data sets of previous studies[31,49].

Statistical and bioinformatics analyses. For computational prediction of miRNAs targeting *ZFAND2B*, a combination of the following software was used: TargetScan (http://www.targetscan.org) and miRanda (http://www.microrna.org). All the experiments were performed at least in independent triplicates (unless noted otherwise) and statistical analyses were derived from these data. All comparisons between WT and knockout mice were performed in animals of the same age. Experimental conditions were blinded and randomized, and no statistical method was used to predetermine sample size. Differences between groups were assayed using Microsoft Excel, SPSS and GraphPad Prism. In all cases, experimental data assumed *t*-test requirements (normal distribution and similar variance); in those cases where the assumption of the *t*-test was not valid, a non-parametric statistical method was used (for example, Wilcoxon signed-rank test). Significant differences were considered when $*P < 0.05$ and $**P < 0.01$. Error bars indicate the s.e.m., as indicated in figure legends.

Accession numbers. RNA expression data are available at the Gene Expression Omnibus repository (GSE71922). Reanalyzed microarray data sets are available at the Gene Expression Omnibus repository (GSE42042, ref. 31; GSE44961, ref. 48; GSE53482, ref. 49). Exome-sequencing raw data are accessible at NCBI Sequence Read Archive (SRA) repository (SRP062260).

37. Liu, P., Jenkins, N.A. & Copeland, N.G. A highly efficient recombineering-based method for generating conditional knockout mutations. *Genome Res.* **13**, 476–484 (2003).
38. Li, J. *et al.* JAK2V617F impairs hematopoietic stem cell function in a conditional knock-in mouse model of *JAK2*V617F-positive essential thrombocythemia. *Blood* **116**, 1528–1538 (2010).
39. Porta-de-la-Riva, M., Fontrodona, L., Villanueva, A. & Cerón, J. Basic *Caenorhabditis elegans* methods: synchronization and observation. *J. Vis. Exp.* **64**, e4019 (2012).
40. Rual, J.F. *et al.* Toward improving *Caenorhabditis elegans* phenome mapping with an ORFeome-based RNAi library. *Genome Res.* **14** 10B, 2162–2168 (2004).
41. Kamath, R.S. & Ahringer, J. Genome-wide RNAi screening in *Caenorhabditis elegans*. *Methods* **30**, 313–321 (2003).
42. Wernig, G. *et al.* Expression of *Jak2*V617F causes a polycythemia vera–like disease with associated myelofibrosis in a murine bone marrow transplant model. *Blood* **107**, 4274–4281 (2006).
43. Rybak, A. *et al.* A feedback loop comprising *lin*-28 and *let*-7 controls pre-*let*-7 maturation during neural stem-cell commitment. *Nat. Cell Biol.* **10**, 987–993 (2008).
44. Scott, L.M. *et al.* JAK2 exon 12 mutations in polycythemia vera and idiopathic erythrocytosis. *N. Engl. J. Med.* **356**, 459–468 (2007).
45. Villarroya-Beltri, C. *et al.* Sumoylated hnRNPA2B1 controls the sorting of miRNAs into exosomes through binding to specific motifs. *Nat. Commun.* **4**, 2980 (2013).
46. Soria-Valles, C. *et al.* NF-κB activation impairs somatic cell reprogramming in aging. *Nat. Cell Biol.* **17**, 1004–1013 (2015).
47. Puente, X.S. *et al.* Noncoding recurrent mutations in chronic lymphocytic leukemia. *Nature* **526**, 519–524 (2015).
48. Mullally, A. *et al.* Depletion of *Jak2*V617F myeloproliferative neoplasm–propagating stem cells by interferon-α in a murine model of polycythemia vera. *Blood* **121**, 3692–3702 (2013).
49. Norfo, R. *et al.* miRNA-mRNA integrative analysis in primary myelofibrosis CD34+ cells: role of miR-155–*JARID2* axis in abnormal megakaryopoiesis. *Blood* **124**, e21–e32 (2014).